RESEARCH ARTICLE

ADVANCED OPTICAL MATERIALS
www.advopticalmat.de

Single Photon Emitters in Hexagonal Boron Nitride Fabricated by Focused Helium Ion Beam

Guan-Lin Liu, Xin-Yu Wu, Peng-Tao Jing, Zhen Cheng, Da Zhan, Yang Bao, Jia-Xu Yan, Hai Xu, Li-Gong Zhang, Bing-Hui Li, Ke-Wei Liu, Lei Liu,* and De-Zhen Shen**

The 2D layered hexagonal boron nitride (hBN) material is a promising platform for making single photon emitters (SPEs). Integrate SPEs with photonic cavities or waveguides, requires the deterministic positioning of these emitters as accurately as possible. Among all of the alternative techniques, He$^+$ focused ion beam (FIB) theoretically has sub-nanometer precision, but its practical positioning accuracy in processing SPEs is limited by the inevitable detrimental byproduct defects. So far, it remains challenging to achieve an accuracy below 100 nm for the positioning of SPEs in hBN. Here, we present a two-step method for creating SPEs at the predetermined positions in hBN that combines the He$^+$ FIB irradiation and thermal annealing under an oxygen atmosphere. With this method, we have realized the positioning accuracy of less than 50 nm, which, to the best of our knowledge, stands as the highest among the currently available hBN SPEs preparation methods. Moreover, the SPE conversion yield was over 35% and the emission brightness of individual SPE achieved up to 3 × 10^5 counts/s at room temperature. These SPEs fabricated precisely with nanoscale accuracy in hBN are expected to be good candidates for making large-scale integrated SPEs in photonic circuits.

1. Introduction

Solid-state quantum emitters are the fundamental component in various photonic quantum technologies,[1] such as quantum communication, quantum sensing, and quantum imaging.[2] In hBN, a wide-bandgap (≈6 eV) 2D layered semiconductor, its optically active defects, namely color centers, have been taken as a good source to make SPEs due to their robust and bright emission at room temperature.[3] As embedded in 2D materials, it is feasible to integrate these hBN SPEs into photonic cavities and waveguides,[4] under the premise that their spatial locations can be precisely controlled. So far, there have been many efforts to generate position-controlled SPEs in hBN,[5] such as nanoindentation with atomic force microscope (AFM),[5a] electron beam irradiation,[5b] Ga$^+$ focused ion beam (FIB),[5c] patterned mask,[5d,e] femtosecond laser writing,[5f] and nanopillars array.[5g] Nevertheless, despite these attempts, it still remains challenging to realize the effective fabrication of defective SPEs in hBN due to the lack of enough control to position them precisely. Normally, the positioning precision of SPEs is required as accurate as much below 100 nm for their practical integration in large-scale photonic quantum devices, such as ≈30 nm for quantum dots,[6] 40–50 nm for color centers in diamond.[7–9] In comparison with other techniques, the He$^+$ FIB provides a more accurate tool for fabricating SPEs in semiconductors, which can theoretically reach sub-nanometer positioning accuracy with the high-resolution helium ion microscope (HIM) imaging function.[10] For example, the He$^+$ FIB has been used to produce SPEs in the bulk SiC crystal.[11] But as the He$^+$ ions penetrate deeply inside the crystal, significant lattice damage will result due to the inelastic collision processes[11,12], and that deteriorate significantly the positioning accuracy of the processed SPEs. As for the layered 2D materials, such concomitant lattice damage can be relieved to a large extent, as most of the excessive ion energy of He$^+$ ions after passing through 2D layers will be absorbed by the substrate below. It has been found that the He$^+$ FIB can produce individual point defects in monolayer MoS$_2$ with the positioning accuracy of ≈9 nm,[13] and such defects have been used to generate SPEs.[14] In the case of hBN, so far, He$^+$ FIB is still unavailable in precisely making actual SPEs, though this technique has been successfully used in producing the boron vacancy spin defects there. This has been attributed to the large amount of byproduct defects produced around the He$^+$ FIB irradiated spots,[15] making them invalid for single photon emitting.

Here, we present a two-step method that creates SPEs at designed positions in hBN by combining He$^+$ FIB irradiation with proper thermal annealing under an oxygen atmosphere. In the

---

G.-L. Liu, X.-Y. Wu, P.-T. Jing, Z. Cheng, D. Zhan, Y. Bao, J.-X. Yan, H. Xu, L.-G. Zhang, B.-H. Li, K.-W. Liu, L. Liu, D.-Z. Shen
State Key Laboratory of Luminescence and Applications
Changchun Institute of Optics
Fine Mechanics and Physics
Chinese Academy of Sciences
Changchun 130033, P. R. China
E-mail: jingpt@ciomp.ac.cn; liulei@ciomp.ac.cn; shendz@ciomp.ac.cn

G.-L. Liu, X.-Y. Wu
University of Chinese Academy of Sciences
Chinese Academy of Sciences
Beijing 100049, P. R. China

The ORCID identification number(s) for the author(s) of this article can be found under https://doi.org/10.1002/adom.202302083

DOI: 10.1002/adom.202302083

first step, position-controlled lattice damages were produced in hBN by He$^+$ FIB. The induced spots of damaged lattice exhibited broad photoluminescence (PL) spectra, without the single photon emission property. In the second step, these FIB fabricated luminescent spots were converted to SPEs after a thermal annealing process with high temperature and oxygen atmosphere. The positioning accuracy of these SPEs was determined to be less than 50 nm, i.e., the full width at half maximum (FWHM) of the irradiated spot. By eliminating the byproduct defects, a high SPE creation yield (>35%) and bright emission (up to 3×10^5 counts/s) at room temperature has been achieved for individual SPE. To our best knowledge, this work proposes a two-step strategy to successfully generate position-controlled SPEs in hBN crystal via He$^+$ FIB for the first time. These position-controlled SPEs in hBN with nanoscale accuracy open up new possibilities for advancing quantum technologies.

2. Results and Discussion

The imaging and milling of the hBN sample with He$^+$ FIB were schematically shown in **Figure** 1a. Before the He$^+$ FIB nanofabrication, exfoliated few-layer hBN flakes were cleaned in ozone to remove tape residue (see methods), but this treatment will cause a broad background fluorescence. This background fluorescence could be eliminated by heating the sample in air over 200 °C, as shown in Figure S1 (Supporting Information). The HIM image of a clean exfoliated few-layer hBN is shown in Figure 1b, which is based on the secondary electrons emitted from inelastic collisions between the He$^+$ ions and the sample. The optimal probe size under an acceleration voltage of 30 kV and beam current of 0.5 pA could be smaller than 1 nm. Under the low He$^+$ dose (10^1–10^2 ions/pixel) for imaging, no obvious damage was induced in the hBN lattice, as shown by the AFM and fluorescence profiles of the hBN flakes before and after HIM imaging (see Figure S2, Supporting Information).

Surface sputtering atoms and lattice damages will be produced by He$^+$ FIB with higher doses beyond that for imaging. Due to the low mass of B and N atoms, significant amounts of energy can be transferred through elastic collisions with He$^+$ ions, similar to the situation with graphene. [10a,16] These lattice damages were estimated less than that induced by Ne$^+$, Xe$^+$, and Ga$^+$ FIB, due to the low mass of He$^+$ ions. [5c,10a,16] He$^+$ FIB was set to the irradiated spots one by one according to a designed array with increasing doses of 1×10^6, 5×10^6, 1×10^7, 2×10^7, 4×10^7, 6×10^7, 8×10^7, 1×10^8 and 2×10^8 ions/spot, as marked in Figure 1b. The fluorescence mapping image of the irradiated sample (Figure 1c) was obtained with our home-made confocal microscope. The observed luminescent spot array, with the inter-spot spacing of 3 μm, is consistent with the FIB fabricated pattern. Individual luminescent spots were repositioned by a piezo stage to record their PL spectra. These artificially fabricated spots on hBN exhibited broad luminescent peaks (Figure 1d), possibly originating from ensembles of the B or N vacancies caused by He$^+$ ion irradiation. The intensities of these luminescent spots were increased with increasing ion doses, as shown in Figure 1e, indicating more defects were induced under higher He$^+$ ions dose. Antibunching phenomenon in second-order autocorrelation function measurement is an important criterion for determining single photon emission.[1a,3a,b] Unfortunately, the antibunching phenomenon was not observed by our home-built Hanbury-Brown-Twiss (HBT) interferometer, as shown in Figure 1f. It means the luminescent spots directly produced by He$^+$ FIB irradiation do not show a single photon emission property.

To evaluate the impact of different He$^+$ ions doses on the hBN lattice structure, we performed AFM measurements of the irradiated hBN samples. AFM topography images for doses of 1×10^6, 6×10^7, and 2×10^8 ions/spot are shown in Figure 1g–i, respectively. AFM images for other doses are shown in Figure S3 (Supporting Information). The thickness of this hBN sample is 21.9 nm. After irradiation via He$^+$ FIB under doses in the range of 1×10^6–$2{\times}10^8$ ions/spot at the acceleration voltage of 30 kV, the crater-like spots of lattice damage were observed on the hBN surface. Each crater-like spot contains a "ring mountain" of sputtered atoms and a milled pit at the center. With increasing He$^+$ ions doses, the depth of the milled pit relative to the hBN plane changed from −0.85 to 3.3 nm (Figure S3, Supporting Information). On the other hand, the shapes and diameters of the craters were almost the same for different doses, indicating the reproducibility of the FIB fabricated spots. In previous literature, the FIB-produced defects were divided into four categories, including single vacancies, double vacancies, complex vacancies, and amorphizations.[10a,16] Moreover, based on molecular dynamics simulations, single vacancies (both B and N) were identified as the dominant types of defects created by He$^+$ ions when the beam is directed perpendicular to the hBN plane.[16] Therefore, direct use of these FIB-induced hBN lattice damages as quantum emitters seems to be infeasible. Nevertheless, such FIB-induced defects provide a highly reproducible nanoscale platform for further modification and functionalization.

Thermal annealing has been widely employed as a method for activating SPEs in hBN. [3a,17] Therefore, the effects of thermal annealing (800–1100 °C) on pristine hBN flakes were explored in Ar, H_2, and O_2 atmospheres, corresponding to inert, reducing, and oxidizing atmospheres (Figure S4, Supporting Information), respectively. Randomly distributed SPEs were only observed in hBN samples annealed in the oxygen atmosphere over 1000 °C, but not with the Ar or H_2 atmospheres. This result suggests that oxygen may play an important role in the activation of SPEs in hBN under thermal annealing.[17a]

The FIB-fabricated hBN samples were similarly treated by thermal annealing in an oxygen atmosphere. The He$^+$ FIB irradiated spot array contains nine rows from top to bottom, with the doses of 1×10^6, 5×10^6, 1×10^7, 2×10^7, 4×10^7, 6×10^7, 8×10^7, 1×10^8 and 2×10^8 ions/spot, respectively. **Figure** 2a–c shows PL mapping images of the hBN flakes with thermal annealing temperatures of 900, 1050, and 1150 °C, respectively. After 900 °C annealing, the PL emission of spots with doses below 8×10^7 ions/spot disappeared after treatment. Broad PL emission spectra were observed for the remaining luminescent spots, similar to the background luminescence of the unprocessed area, as shown in Figure 2d. The critical temperature for generating random SPEs in hBN was found to be 1000–1100 °C. In consideration of the higher activity of the FIB fabricated spots, the annealing temperature of 1050 °C was selected to treat the FIB irradiated samples. Luminescent spots with irradiation dose lower than 2×10^7 ions/spot were barely identified in the PL mapping image. It was found that only samples processed within a

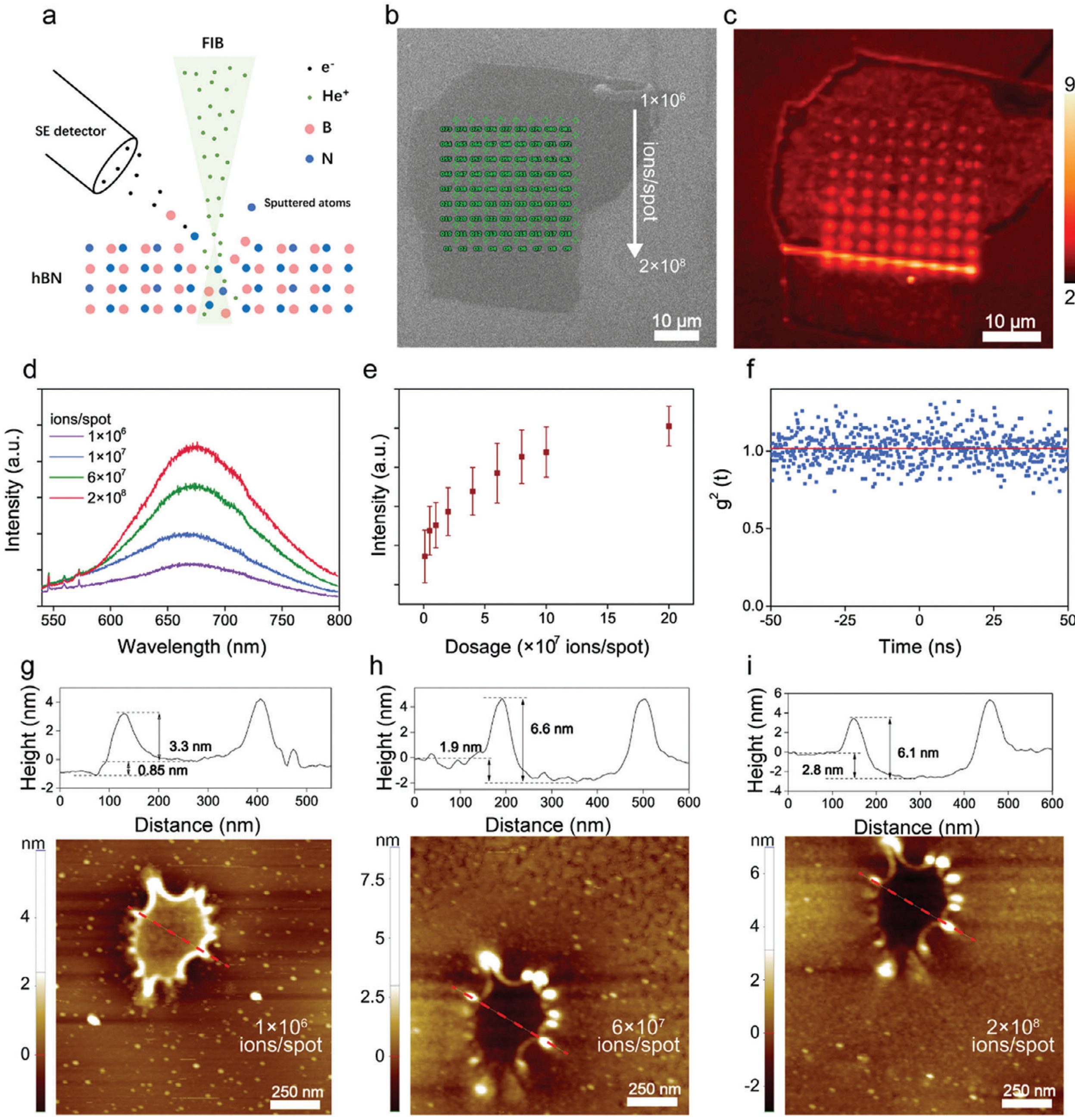

Figure 1. a) Schematic diagram of irradiation of hBN sample with He$^+$ FIB. Green and black dots represent He$^+$ ion and secondary electron (SE). Pink and blue solid-line circles represent B and N atoms. b) HIM image and c) PL emission intensity mapping image of the array on hBN sample after irradiation of He$^+$ FIB with different doses. d) PL Spectra of luminescent spots on hBN sample after irradiation of He$^+$ FIB with different doses. e) PL intensity of luminescent spots versus irradiation dose. f) Second order correlation function measurement for emitter on hBN sample after irradiation of He$^+$ FIB with doses of 6×10^7 ions/spot. Excitation laser wavelength and power are 532 nm and ≈100 μW. AFM topography images of hBN sample after irradiation of He$^+$ FIB, respectively for doses of g) 1×10^6, h) 6×10^7, and i) 2×10^8 ions/spot.

certain range of doses, specifically between 2×10^7 and 8×10^7 ions/spot, exhibited light emission with narrow PL peak, as show in Figure 2e. Furthermore, the background luminescence was suppressed under this treatment condition. At higher or lower He$^+$ ion doses, even with this optimal thermal annealing condition, the irradiated spots will not contribute to single photon emission. For lower doses, PL emission disappeared after thermal annealing, likely due to the thermally induced self-healing of the He$^+$ ion-induced hBN defects. In contrast, for higher dose samples, we encountered difficulties in isolating individual SPE due to the creation of too many quantum emitters in the same irradiation spot. After thermal annealing at 1150 °C, the hBN flake was obviously ablated over a large area due to extensive oxidation (Figure 2c), causing the FIB fabricated spots array to be

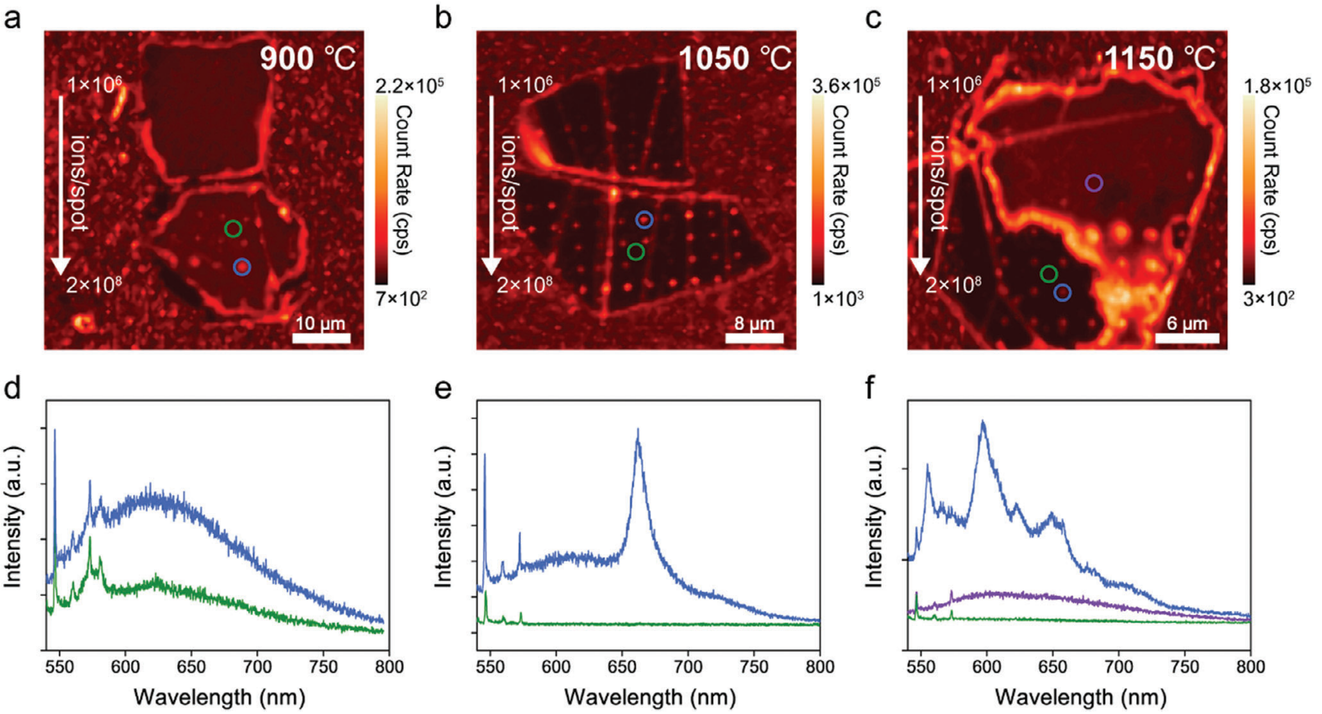

Figure 2. PL emission intensity mapping image of the array on hBN sample after irradiation of He^+ FIB with different doses, after thermal annealing with oxygen atmosphere under different temperatures of a) 900 °C, b) 1050 °C, and c) 1150 °C. d–f) PL spectra of fabricated luminescent spot and background as color cycles marked in images (a), (b), and (c).

destroyed. Figure 2f shows that the remaining luminescent spots contain multiple narrow peaks, indicating the formation of multiple color centers at the processed site. Moreover, the background luminescence was enhanced at the ablated area, in comparison to that at the normal unprocessed hBN area. Consequently, He^+ FIB doses of 2×10^7–8×10^7 ions/spot and a thermal annealing temperature of 1050 °C represent the optimal experimental conditions for further exploration.

The conditions for activating the SPEs in hBN were optimized by adjusting parameters such as He^+ ion dose, annealing temperature, annealing duration, and oxygen gas flow rate. **Figure 3a** shows the fluorescence mapping results of an hBN flake (He^+ ions dose of 6×10^7 ions/spot, acceleration voltage of 30 kV, thermal annealing at 1050 °C for 60 min, the oxygen flow rate of 500 sccm, tube furnace is vacuum pumped). Under the excitation of 532 nm laser line, Figure 3b depicts PL spectra of several luminescent spots in the FIB fabricated arrays with narrow peaks of 553, 593, 616, 637, and 687 nm, respectively. Typically, the spectra of these FIB fabricated emitters are characterized by their profiles of single photon emission. For example, it is clearly observed a sharp PL emission peak at 616 nm and a side emission peak at 670 nm, corresponds to zero phonon line (ZPL) and phonon sideband (PSB). The energy differences between ZPLs (553, 593, 616, 637, and 687 nm) and corresponding PSBs are 176, 169, 162, 175, and 163 meV, respectively, which match well with the in-plane optical phonon (E_{2g}) energy of hBN (≈170 meV, see Raman spectrum in Figure S5, supporting information).[18] The PL emission of some luminescent spots was very close to the excitation laser line (532 nm), as shown in Figure S6 (Supporting Information). Half the PL emission peak of this luminescent spot was cut off by an edge filter. To evaluate if these spots are potential SPEs, their PL spectra excited by the 473 nm laser line were obtained (Figure 3c). More ZPL emission spectra of SPEs were found under the excitation of the 473 nm laser. The ZPL peaks of these SPEs are 500, 504, 507, 515, and 538 nm, and their PSB peaks are 537, 541, 544, 550, and 579 nm, respectively. The energy differences between ZPLs and corresponding PSBs are 171, 168, 166, 153, and 163 meV, respectively, as well as due to the coupling between the emission dipole and the in-plane optical phonon (E_{2g}).

Antibunching phenomena were observed in PL emission spots of the fabricated array, as shown in Figure 3d,e and Figure S7 (Supporting Information) in supporting information. The measured $g^2(0)$ values of representative emitters were observed below 0.5, indicating SPEs were successfully fabricated via this two-step method. The experimental $g^2(\tau)$ data are fitted using a two-level model: $g^2\ (t) = 1 - a\, e^{-|t|/\tau}$, where parameter a is the fitting parameter and τ is the fitted fluorescence lifetime of the emitter.[18a,3b] The fitted values of τ are 2.6 and 3.7 ns for SPEs with ZPL peaks of 507 and 616 nm, respectively. These SPEs exhibited antibunching phenomena with $g^2(0)$ values of 0.18 and 0.12, respectively. The wavelength statistical analysis of the quantum emitters is presented in Figure 3f. The SPEs with ZPL wavelength above 550 nm are not suitably excited by a 473 nm laser, because the fluorescence background is enhanced under excitation of a shorter wavelength laser line (See Figure S8, Supporting Information). After thermal annealing, over 35% of the luminescent spots were successfully converted to SPEs, based on the second-order autocorrelation function measurement. A large proportion (65%) of the luminescent spots were not converted

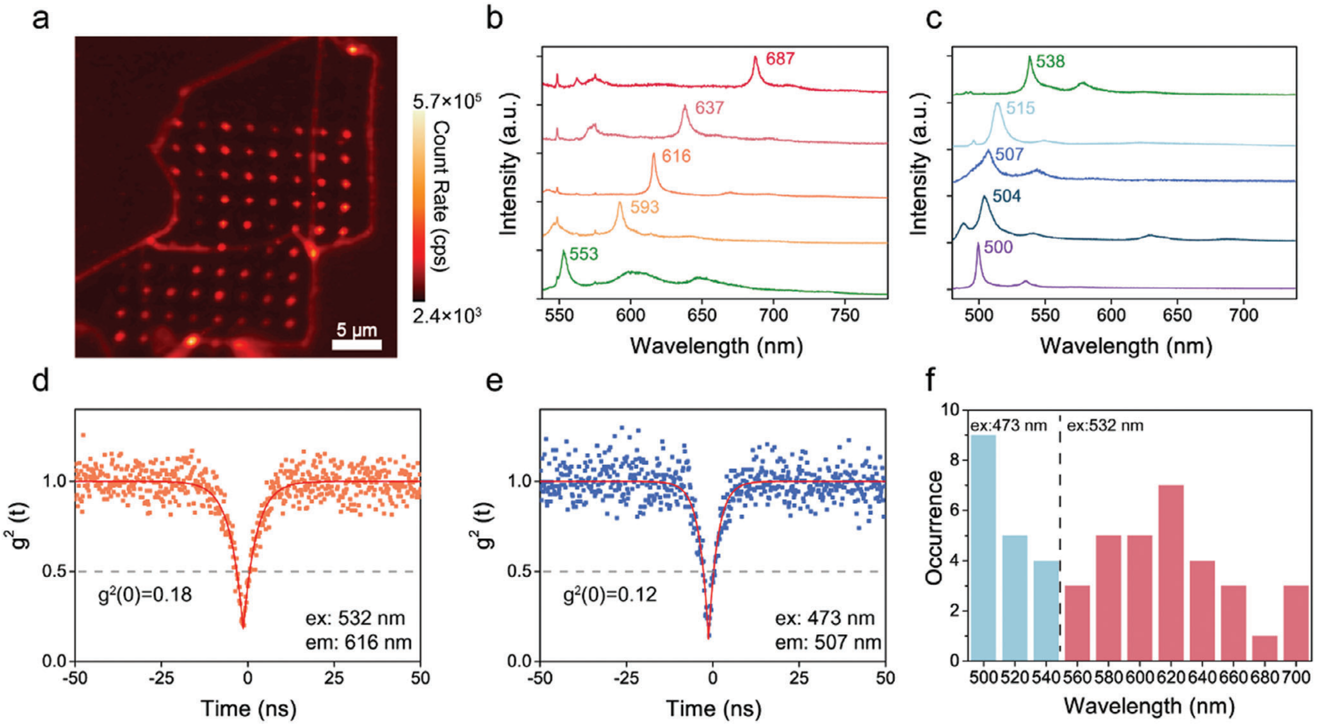

Figure 3. a) PL emission intensity mapping in SPE array on hBN sample after thermal annealing treatment. The spacing between adjacent spots is 3 µm. b) PL Spectra of SPEs on hBN sample. Excitation laser wavelength and power are 532 nm and ≈100 µW. c) PL Spectra of SPEs on hBN sample. Excitation laser wavelength and power are 473 nm and ≈100 µW. Second-order correlation function measurement for SPE on hBN sample with an emission peak wavelength of d) 616 nm and e) 507 nm. f) cBlue bars were excited by 473 nm laser, and red bars were excited by 532 nm laser.

to SPEs. The possible reason is that the vigorous oxidation reaction under a high-temperature annealing process reduces the SPE conversion yield. The conversion yield would be improved under relatively mild annealing conditions by replacing oxygen with oxygen plasma. As seen in Figure 3f, SPEs with emission bands at 500 ± 10 nm (2.48 eV) and 620 ± 10 nm (2.00 eV) were the most frequently observed ones. The above experimental results show that the position-controlled SPEs in hBN have been successfully fabricated by this two-step method.

To explore changes in the hBN surface topography before and after thermal annealing processing in oxygen, we characterized the samples using AFM, as shown in **Figure** 4a,b. The thickness of this hBN sample is 42.9 nm. The crater's shapes were almost the same before and after thermal annealing. It should be noted that the depth of the crater was changed from 5.0 to 3.5 nm after thermal annealing. Additionally, it was clearly observed that some small shallow triangle-shaped voids were formed around the FIB fabricated crater after thermal annealing in an oxygen atmosphere. The formation of these triangle-shaped voids is probably due to the continuous oxidization etching under high temperatures over 1000 °C.[19] It can be inferred that these triangular voids were oxygen-terminated defects.[16,19c,20] The depth of these voids was ≈0.61 nm, as shown in Figure S9 (Supporting Information). The density of these voids was estimated above 140 μm^{-2}. Nevertheless, PL emission was not observed in these triangle-shaped voids. The FIB fabricated hBN sample was washed with deionized water. After this process, the ring mountain disappeared, but the pit remained, as seen in the AFM topography image in Figure 4c. The depth of this pit is 4.5 nm, induced by He^+ FIB milling. The ring mountain around the pit is resulted from the sputtered atoms. The Gaussian-fitted lateral FWHMs of individual FIB fabricated pit are 37.3 and 36.9 nm, respectively for vertical and horizontal cross profiles (Figure 4d). Moreover, after water cleaning, the processed SPEs remain stable with sharp PL spectra and good single photon emission property. It can be inferred that the SPE is, in all probability, formed inside the pit rather than the ring mountain.

In this work, we take a two-step strategy to successfully prepare SPEs in hBN flakes, as schematically shown in Figure 4e. The first step is to produce some lattice damage on the surface of hBN by using He^+ FIB. A crater-like spot of lattice damage with a diameter of ≈100 nm was observed by AFM measurements. The calculated lateral straggling is ≈57 nm for 30 keV He^+ ions implantation into hBN, simulated from the stopping and range of ions in matter (SRIM) software. [7,11,21] The He^+ FIB-produced craters exhibit broad PL emission peaks and no single photon emission property. Then the crucial second step is to anneal the sample in oxygen, so that highly active defects inside those craters may react with oxygen under high temperatures to form color centers in hBN that give bright and stable single photon emission. It was also found that to successfully activate the SPEs, hBN samples after the FIB fabricating process need to be sent to thermal annealing immediately before the highly active defects were chemically deactivated by air or water vapor. The temperature and oxygen atmosphere are crucial factors in activating the FIB-induced lattice damages to SPEs. The oxygen molecules under

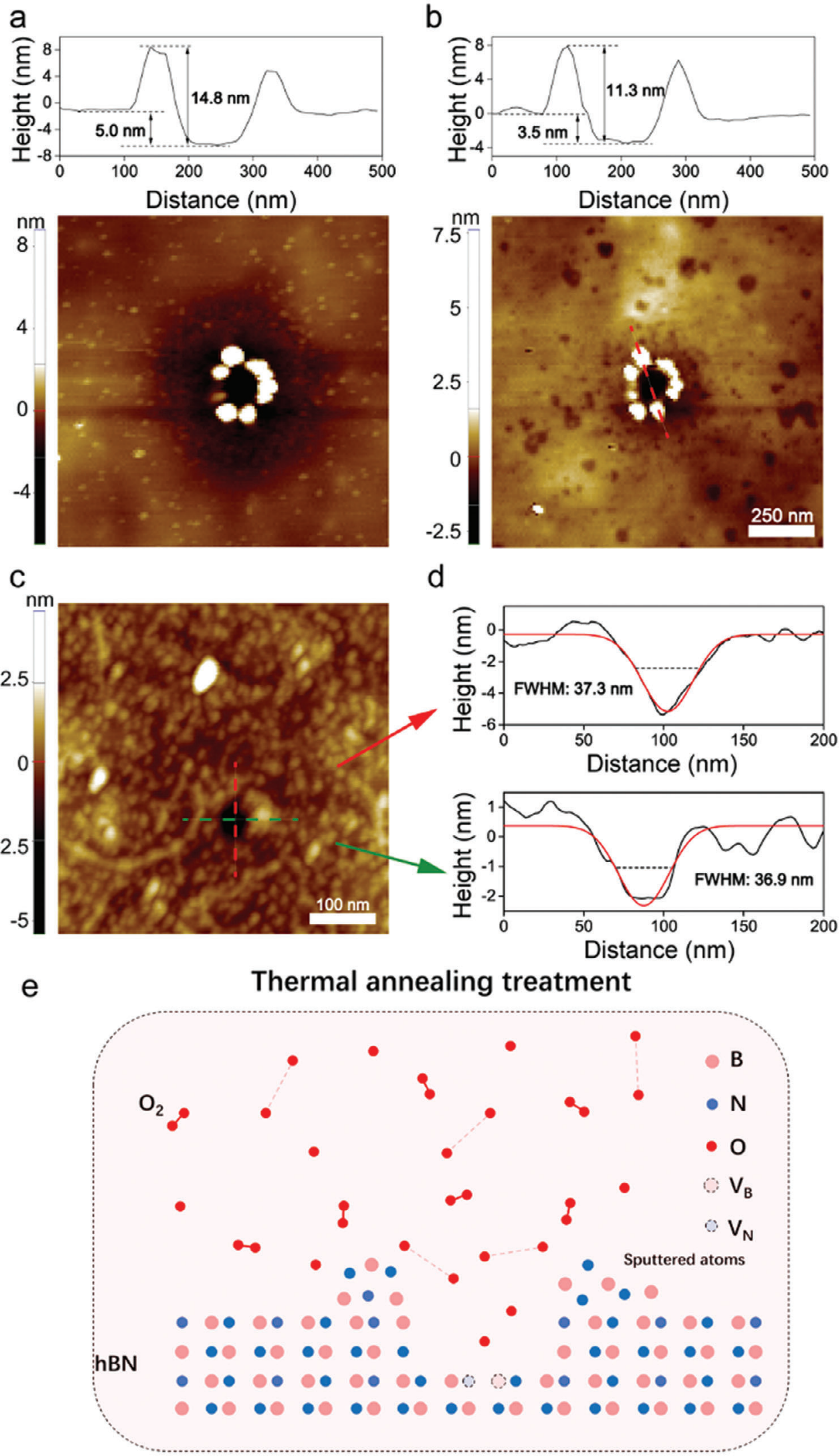
a
Height (nm)
8
4
0
-4
-8
14.8 nm
5.0 nm
0
100
200
300
400
500
Distance (nm)
b
Height (nm)
8
4
0
-4
11.3 nm
3.5 nm
0
100
200
300
400
500
Distance (nm)
nm
8
4
0
-4
nm
7.5
5
2.5
0
-2.5
250 nm
c
nm
2.5
0
-2.5
-5
100 nm
d
Height (nm)
0
-2
-4
-6
FWHM: 37.3 nm
0
50
100
150
200
Distance (nm)
Height (nm)
1
0
-1
-2
FWHM: 36.9 nm
0
50
100
150
200
Distance (nm)
e
Thermal annealing treatment
O_2
B
N
O
V_B
V_N
Sputtered atoms
hBN

Figure 4. AFM topography images of He$^+$ FIB fabricated spot on hBN sample before a) and after b) thermal annealing treatment. The cross profiles of fabricated craters on hBN samples, as marked in figures. c) AFM topography image of FIB fabricated spot on hBN after water cleaning. d) The cross profiles of the spot and Gaussian fitting lines. The irradiation dose for the above sample was 6×10^7 ions/spot. e) Schematic diagram of thermal annealing treatment for He$^+$ FIB fabricated hBN sample with oxygen atmosphere. Pink and blue solid-line circles represent B and N atoms. Pink and blue dotted-line circles represent B vacancy (V_B) and N vacancy (V_N). Double red solid-line circles linked together represent oxygen molecules (O_2). A red solid-line circle represents oxygen atoms (O).

high temperatures (1050 °C) will dissociate into oxygen atoms.[22] Oxygen atoms are probably incorporated into the areas locally irradiated by He$^+$ FIB. When the FIB irradiation dose is below 2×10^7 ions/spot, no luminescent array is observed after thermal annealing in oxygen, probably because oxygen-incorporated complex defects were not formed. When FIB irradiation dose is too high above 1×10^8 ions/spot, multiple oxygen-incorporated complex defects were formed in the same FIB irradiated pit, leading to luminescent spots that exhibit multiple peaks and $g^2(0)$ values above 0.5. These phenomena indicate that FIB irradiation provides more active sites for involving oxygen-incorporated complex defects.[23] Under suitable FIB dosage and appropriate conditions of thermal annealing in an oxygen atmosphere, SPE sources can be deterministically produced in hBN crystal.

After determining the quantum emission properties of these artificial defects, a more detailed analysis was conducted in order to demonstrate the application potential in quantum chip integration. **Figure** 5a exhibits the spectral stability test of the SPE fabricated by this two-step method. Spectral diffusion was not observed under an excitation power of 0.1 mW for 600 s, providing evidence of the excellent stability of the processed SPE. Moreover, stable single photon emission can still be observed even after the sample has been exposed to the air for over 100 days. Figure 5b depicts the excitation power-dependent emission intensity of the individual SPE. The experimental data were fit using the equation: $I = I_\infty \times P/(P + P_{sat})$, where I_∞ and P_{sat} are the emission rate and excitation power at saturation, respectively.[3a] Our direct measurements provide a fitting result of yields $I_\infty \approx 3.3 \times 10^5$ cps and $P_{sat} \approx 2.5$ mW, comparable to values obtained from other preparation methods.[5b] Due to the limitation of light collection efficiency, the actual brightness of individual SPE should exceed 10^6 cps.

The linear excitation and emission polarizations were observed in the polarized fluorescence measurements with varying the polarization angle of the laser and polarizer, as displayed in Figure 5c and Figures S12–15 (Supporting Information). The fluorescence intensity is fitted by $I(\theta) = A \cdot \cos^2(\theta - \alpha) + B$, where α is the polar angle of the normalized absorption or emission dipole moment μ, θ is the polar angle of the excitation and emission electric field E, A, and B are the fitting parameters.[3a,18b] The polar angle θ of excitation or emission was varied by rotation of a half-wave-plate or polarizer. The emission is linearly polarized, suggesting a single dipole transition linearly oriented in the basal plane of the hBN crystal. The degree of polarization is the ratio of the polarized part of the intensity to the total. The measured degree of polarization is defined as $\Pi = (I_{max}-I_{min})/(I_{max}+I_{min})$, where I_{max} and I_{min} are the maximum and minimum intensity of the measured polarized fluorescence. [24] The degree of polarization was measured between 0.55 and 0.89, with an average of 0.72. The unpolarized part of intensity is due to the background luminescence. The polar angles of excitation and emission for individual SPE were the same or different, indicating the direct or indirect absorption process, as seen in Figures S13,S14 (Supporting Information), respectively. In addition, two SPEs with different polar angles were contained in the same luminescent spot, as seen in Figure S15 (Supporting Information), resulting from multiple SPEs that were activated in the same FIB fabricated spot after thermal annealing with oxygen atmosphere.

3. Conclusion

In summary, we have demonstrated a two-step method combining He$^+$ FIB irradiation with thermal annealing in an oxygen atmosphere to achieve position-controlled SPEs in hBN. In the first step, the lattice damages in the form of arrayed spots were directionally introduced by He$^+$ FIB irradiation with the dose of 2×10^7–8×10^7 ions/spot. While possessing broad PL spectra,

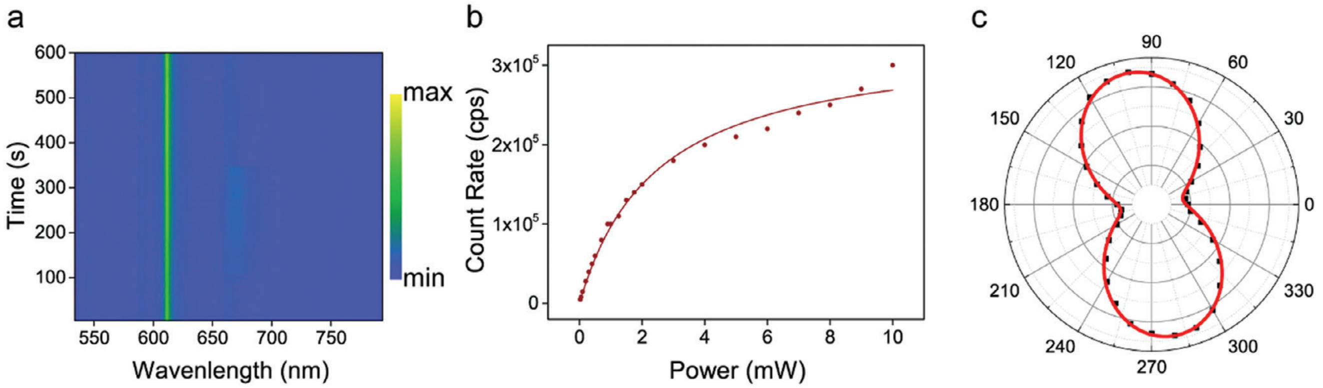

Figure 5. a) PL spectra trace as a function of duration time ≈600 s. The excitation wavelength is 532 nm, and the power is 100 μW. b) Emission count rate of SPE on hBN versus excitation laser power. The solid line is the fitting curve as described in the article. c) PL intensity as a function of the polarization angle of the excitation laser.

these induced spots of damaged lattice do not show single photon emission properties. In the second step, with the help of the 1050 °C thermal annealing in an oxygen atmosphere, the destructive byproduct defects were suppressed and that converted effectively these luminescent spots into SPEs. This method has enabled the deterministic creation of SPEs in hBN at a high precision of less than 50 nm, and with a high creation yield of above 35%. The emission brightness of these artificial SPEs could reach up to 3×10^5 cps at room temperature. Being bright, stable, and precisely positioned, these FIB-fabricated hBN SPEs are expected to play an important role in photonic quantum devices.

4. Experimental Section

Sample Fabrication and Characterization: The hBN flakes were mechanically exfoliated from bulk crystal (Onway) on SiO_2/Si substrates with 300 nm thick silicon dioxide and preprepared markers. The flakes were cleaned using a UV-Ozone cleaner (Setcas, SC-UV-I) for 30 min to remove tape residues. The hBN samples were milled by a focused helium ion beam (Zeiss, Orion Nanofab), where the acceleration voltage and beam current were set to 30 kV and 1.9 pA, and the dwell time was adjusted to obtain desired doses. Then, the samples were subjected to high temperature (800–1150 °C) annealing for 30–60 min under hydrogen, oxygen, or argon atmosphere. AFM measurements were performed on an atomic force microscope (Park NX10).

Optical Measurements: The samples were characterized on a home-built confocal optical microscope with functions of spectral measurements, polarization testing, and anti-bunching testing. The excitation source was 473 or 532 nm CW lasers (Changchun New Industries Optoelectronics), which were induced into the microscope by using a dichroic mirror and focused onto the sample through a 100× objective lens with NA of 0.95 (Olympus). The fluorescence signal after the long-pass filter was collected into the optical fiber and transferred to an imaging spectrometer with a liquid nitrogen-cooled camera (Princeton Instruments, IsoPlane-320A, and PyLoN 400B) or HBT equipment with two SPADs (Excelitas, SPCM-AQRH-14-TR). The antibunching measurements were performed on a time-correlated single photon counting module (PicoQuant, MultiHarp 150).

Supporting Information

Supporting Information is available from the Wiley Online Library or from the author.

Acknowledgements

This work was supported by the National Natural Science Foundation of China (Grant No.: 11727902, 12074372, 12174385, 62074148) and the 100 Talents Program of the Chinese Academy of Sciences.

Conflict of Interest

The authors declare no conflict of interest.

Data Availability Statement

The data that support the findings of this study are available from the corresponding author upon reasonable request.

Keywords

focused helium ion beam, hexagonal boron nitride, single photon emission

Received: August 28, 2023
Revised: November 13, 2023
Published online: November 27, 2023

[1] a) I. Aharonovich, D. Englund, M. Toth, *Nat. Photonics* **2016**, *10*, 631; b) I. Aharonovich, E. Neu, *Adv. Opt. Mater.* **2014**, *2*, 911; c) H. Wang, Y.-M. He, T.-H. Chung, H. Hu, Y. Yu, S. Chen, X. Ding, M.-C. Chen, J. Qin, X. Yang, R.-Z. Liu, Z.-C. Duan, J.-P. Li, S. Gerhardt, K. Winkler, J. Jurkat, L.-J. Wang, N. Gregersen, Y.-H. Huo, Q. Dai, S. Yu, S. Höfling, C.-Y. Lu, J.-W. Pan, *Nat. Photonics* **2019**, *13*, 770; d) X. Ding, Y. He, Z.-C. Duan, N. Gregersen, M.-C. Chen, S. Unsleber, S. Maier, C. Schneider, M. Kamp, S. Höfling, C.-Y. Lu, J.-W. Pan, *Phys. Rev. Lett.* **2016**, *116*, 020401; e) A. Sipahigil, K. D. Jahnke, L. J. Rogers, T. Teraji, J. Isoya, A. S. Zibrov, F. Jelezko, M. D. Lukin, *Phys. Rev. Lett.* **2014**, *113*, 113602; f) Z. Yuan, B. E. Kardynal, R. M. Stevenson, A. J. Shields, C. J. Lobo, K. Cooper, N. S. Beattie, D. A. Ritchie, M. Pepper, *Science* **2002**, *295*, 102.

[2] a) H. Bernien, B. Hensen, W. Pfaff, G. Koolstra, M. S. Blok, L. Robledo, T. H. Taminiau, M. Markham, D. J. Twitchen, L. Childress, R. Hanson, *Nature* **2013**, *497*, 86; b) D. P. D. Charles, H. Bennett, *Nature* **2000**, *404*, 247; c) N. Gisin, R. Thew, *Nat. Photonics* **2007**, *1*, 165; d) T. E. Northup, R. Blatt, *Nat. Photonics* **2014**, *8*, 356; e) J. L. O'brien, A. Furusawa, J. Vuckovic, *Nat. Photonics* **2009**, *3*, 687; f) S. Pirandola, B. R. Bardhan, T. Gehring, C. Weedbrook, S. Lloyd, *Nat. Photonics* **2018**, *12*, 724; g) Z.-P. Li, J.-T. Ye, X. Huang, P.-Y. Jiang, Y. Cao, Y. Hong, C. Yu, J. Zhang, Q. Zhang, C.-Z. Peng, F. Xu, J.-W. Pan, *Optica* **2021**, *8*, 344; h) L. Rondin, J.-P. Tetienne, T. Hingant, J.-F. Roch, P. Maletinsky, V. Jacques, *Rep. Prog. Phys.* **2014**, *77*, 056503.

[3] a) T. T. Tran, K. Bray, M. J. Ford, M. Toth, I. Aharonovich, *Nat. Nanotechnol.* **2016**, *11*, 37; b) M. Toth, I. Aharonovich, *Annu. Rev. Phys. Chem.* **2019**, *70*, 123; c) J. D. Caldwell, I. Aharonovich, G. Cassabois, J. H. Edgar, B. Gil, D. N. Basov, *Nat. Rev. Mater.* **2019**, *4*, 552; d) X. Liu, M. C. Hersam, *Nat. Rev. Mater.* **2019**, *4*, 669; e) A. Sajid, M. J. Ford, J. R. Reimers, *Rep. Prog. Phys.* **2020**, *83*, 044501; f) M. Kianinia, Z.-Q. Xu, M. Toth, I. Aharonovich, *Appl. Phys. Rev.* **2022**, *9*, 011306; g) I. Aharonovich, J.-P. Tetienne, M. Toth, *Nano Lett.* **2022**, *22*, 9227.

[4] a) T. Vogl, R. Lecamwasam, B. C. Buchler, Y. Lu, P. K. Lam, *ACS Photonics* **2019**, *6*, 1955; b) N. V. Proscia, H. Jayakumar, X. Ge, G. Lopez-Morales, Z. Shotan, W. Zhou, C. A. Meriles, V. M. Menon, *Nanophotonics* **2020**, *9*, 2937; c) J. E. Fröch, C. Li, Y. Chen, M. Toth, M. Kianinia, S. Kim, I. Aharonovich, *Small* **2022**, *18*, e2104805; d) C. Li, J. E. Fröch, M. Nonahal, T. N. Tran, M. Toth, S. Kim, I. Aharonovich, *ACS Photonics* **2021**, *8*, 2966.

[5] a) X. Xu, Z. O. Martin, D. Sychev, A. S. Lagutchev, Y. P. Chen, T. Taniguchi, K. Watanabe, V. M. Shalaev, A. Boltasseva, *Nano Lett.* **2021**, *21*, 8182; b) C. Fournier, A. Plaud, S. Roux, A. Pierret, M. Rosticher, K. Watanabe, T. Taniguchi, S. Buil, X. Quélin, J. Barjon, J.-P. Hermier, A. Delteil, *Nat. Commun.* **2021**, *12*, 3779; c) J. Ziegler, R. Klaiss, A. Blaikie, D. Miller, V. R. Horowitz, B. J. Alemán, *Nano Lett.* **2019**, *19*, 2121; d) J. C. Stewart, Y. Fan, J. S. H. Danial, A. Goetz, A. S. Prasad, O. J. Burton, J. A. Alexander-Webber, S. F. Lee, S. M. Skoff, V. Babenko, S. Hofmann, *ACS Nano* **2021**, *15*, 13591; e) N.-J. Guo, S. Li, W. Liu, Y.-Z. Yang, X.-D. Zeng, S. Yu, Y. Meng, Z.-P. Li, Z.-A. Wang, L.-K. Xie, R.-C. Ge, J.-F. Wang, Q. Li, J.-S. Xu, Y.-T. Wang, J.-S. Tang, A. Gali, C.-F. Li, G.-C. Guo, *Nat. Commun.* **2023**, *14*, 2893; f) L. Gan, D. Zhang, R. Zhang, Q. Zhang, H. Sun, Y. Li, C.-Z. Ning, *ACS Nano* **2022**, *16*, 14254; g) C. Li, N. Mendelson, R. Ritika, Y. Chen, Z.-Q. Xu, M. Toth, I. Aharonovich, *Nano Lett.* **2021**, *21*, 3626.

[6] K. Hennessy, A. Badolato, M. Winger, D. Gerace, M. Atatüre, S. Gulde, S. Fält, E. L. Hu, A. Imamoglu, *Nature* **2007**, *445*, 896.

[7] N. H. Wan, T.-J. Lu, K. C. Chen, M. P. Walsh, M. E. Trusheim, L. De Santis, E. A. Bersin, I. B. Harris, S. L. Mouradian, I. R. Christen, E. S. Bielejec, D. Englund, *Nature* **2020**, *583*, 226.

[8] R. E. Evans, M. K. Bhaskar, D. D. Sukachev, C. T. Nguyen, A. Sipahigil, M. J. Burek, B. Machielse, G. H. Zhang, A. S. Zibrov, E. Bielejec, H. Park, M. Loncar, M. D. Lukin, *Science* **2018**, *362*, 662.

[9] A. Sipahigil, R. E. Evans, D. D. Sukachev, M. J. Burek, J. Borregaard, M. K. Bhaskar, C. T. Nguyen, J. L. Pacheco, H. A. Atikian, C. Meuwly, R. M. Camacho, F. Jelezko, E. Bielejec, H. Park, M. Loncar, M. D. Lukin, *Science* **2016**, *354*, 847.

[10] a) G. Hlawacek, A. Gölzhäuser, *Helium Ion Microscopy*, Springer International Publishing, Switzerland, **2016**; b) S. T. Richard Livengood, Y. Greenzweig, J. Notte, S. McVey, *J. Vac. Sci. Technol. B* **2009**, *27*, 3244.

[11] Z.-X. He, Q. Li, X.-L. Wen, J.-Y. Zhou, W.-X. Lin, Z.-H. Hao, J.-S. Xu, C.-F. Li, G.-C. Guo, *ACS Photonics* **2022**, *10*, 2234.

[12] R. Timilsina, D. A. Smith, P. D. Rack, *Nanotechnology* **2013**, *24*, 115302.

[13] E. Mitterreiter, B. Schuler, K. A. Cochrane, U. Wurstbauer, A. Weber-Bargioni, C. Kastl, A. W. Holleitner, *Nano Lett.* **2020**, *20*, 4437.

[14] K. Barthelmi, J. Klein, A. Hötger, L. Sigl, F. Sigger, E. Mitterreiter, S. Rey, S. Gyger, M. Lorke, M. Florian, F. Jahnke, T. Taniguchi, K. Watanabe, V. Zwiller, K. D. Jöns, U. Wurstbauer, C. Kastl, A. Weber-Bargioni, J. J. Finley, K. Müller, A. W. Holleitner, *Appl. Phys. Lett.* **2020**, *117*, 070501.

[15] H. Liang, Y. Chen, C. Yang, K. Watanabe, T. Taniguchi, G. Eda, A. A. Bettiol, *Adv. Opt. Mater.* **2023**, *11*, 2201941.

[16] O. Lehtinen, E. Dumur, J. Kotakoski, A. V. Krasheninnikov, K. Nordlund, J. Keinonen, *Nucl. Instrum. Methods Phys. Res. Sect. B* **2011**, *269*, 1327.

[17] a) Y. Chen, C. Li, S. White, M. Nonahal, Z.-Q. Xu, K. Watanabe, T. Taniguchi, M. Toth, T. T. Tran, I. Aharonovich, *ACS Appl. Mater. Interfaces* **2021**, *13*, 47283; b) H. Ngoc My Duong, M. A. P. Nguyen, M. Kianinia, T. Ohshima, H. Abe, K. Watanabe, T. Taniguchi, J. H. Edgar, I. Aharonovich, M. Toth, *ACS Appl. Mater. Interfaces* **2018**, *10*, 24886.

[18] a) N. R. Jungwirth, B. Calderon, Y. Ji, M. G. Spencer, M. E. Flatté, G. D. Fuchs, *Nano Lett.* **2016**, *16*, 6052; b) N. R. Jungwirth, G. D. Fuchs, *Phys. Rev. Lett.* **2017**, *119*, 057401; c) C. Linderälv, W. Wieczorek, P. Erhart, *Phys. Rev. B* **2021**, *103*, 115421.

[19] a) J. C. Lu Hua Li, K. Watanabe, T. Taniguchi, Y. Chen†, *ACS Nano* **2014**, *8*, 1457; b) N. Khan, J. Li, J. H. Edgar, *MRS Commun.* **2022**, *12*, 74; c) S. P. Huber, E. Gullikson, R. W. E. Van De Kruijs, F. Bijkerk, D. Prendergast, *Phys. Rev. B* **2015**, *92*, 245310.

[20] a) C. Jin, F. Lin, K. Suenaga, S. Iijima, *Phys. Rev. Lett.* **2009**, *102*, 195505; b) P. Valerius, C. Herbig, M. Will, M. A. Arman, J. Knudsen, V. Caciuc, N. Atodiresei, T. Michely, *Phys. Rev. B* **2017**, *96*, 235410.

[21] J. F. Ziegler, M. D. Ziegler, J. P. Biersack, *Nucl. Instrum. Methods Phys. Res. Sect. B* **2010**, *268*, 1818.

[22] G. I. Golodets, in *Studies in Surface Science and Catalysis*, Vol. *15*, Elsevier, Amsterdam **1983**.

[23] a) S. Li, A. Gali, *J. Phys. Chem. Lett.* **2022**, *13*, 9544; b) C. Liang, Y. Sha, J. Huang, C. Zhang, S. Su, H. Li, G. Wang, K. Liu, F. Wang, H. Wang, W. Luo, G. Chen, T. Wu, X. Xie, D. Qian, H. Tao, *J. Phys. Chem. Lett.* **2022**, *13*, 3369; c) S. Gao, H.-Y. Chen, M. Bernardi, *NPJ Comput. Mater.* **2021**, *7*, 85.

[24] C.-H. Teng, L. Zhang, T. A. Hill, B. Demory, H. Deng, P.-C. Ku, *Appl. Phys. Lett.* **2015**, *107*, 191105.